

Improvement of near-surface wind speed modeling through refined aerodynamic roughness length in built-up regions: implementation and validation in the Weather Research and Forecasting (WRF) model version 4.0

Jiamin Wang¹, Kun Yang^{1,2}, Jiarui Liu¹, Xu Zhou³, Xiaogang Ma⁴, Wenjun Tang³, Ling Yuan⁵, Zuhuan Ren¹

¹Ministry of Education Key Laboratory for Earth System Modeling, Department of Earth System Science, Institute for Global Change Studies, Tsinghua University, Beijing 100084, China.

²Renewables Research Center of Huairou Laboratory, Beijing 101499, China.

³National Tibetan Plateau Data Center, State Key Laboratory of Tibetan Plateau Earth System, Environment and Resources, Institute of Tibetan Plateau Research, Chinese Academy of Sciences, Beijing 100101, China.

⁴National Institute of Natural Hazards, Ministry of Emergency Management of China, Beijing, 100085, China.

⁵China State Shipbuilding Corporation Haizhuang Windpower Co., Ltd., Chongqing 401123, China.

Correspondence to: Kun Yang (yangk@tsinghua.edu.cn)

Abstract. Aerodynamic roughness length (z_0) is a key parameter determining near-surface wind profiles, significantly influencing wind-related studies and applications. In built-up areas, surface roughness has been substantially altered by land use changes such as urbanization. However, many numerical models assign z_0 values based on vegetation cover types, neglecting urban effects. This has resulted in a lack of reliable z_0 data in built-up regions. To address this issue, this study proposed a cost-effective method to estimate z_0 values at weather stations by adjusting z_0 values to minimize the wind speed differences between ERA5 reanalysis data and weather station observation data. Using this approach, z_0 values were derived for 1,805 stations in the built-up areas across China. Based on these estimates, a high-resolution monthly gridded z_0 dataset was then developed for built-up areas in China using Random Forest Regression algorithm. Simulations with Weather Research and Forecasting (WRF) model show that implementation of the new z_0 dataset significantly improves the accuracy of 10-m wind speed over built-up areas, reducing mean wind speed errors by 89.9% and 88.9% compared to the default z_0 in WRF and a latest gridded z_0 dataset, respectively. Independent validations of 100-m wind speed against anemometer tower data further confirm the dataset's reliability. Therefore, this approach is valuable for wind-dependent studies and applications, such as urban planning, air quality management, and wind energy utilization, by enabling more accurate simulations of wind speed in built-up areas.

1 Introduction

With the rapid advancement of urbanization and industrialization, urban and town-dominated built-up areas have emerged as the predominant zones for population aggregation and energy consumption (Liu et al., 2014). Built-up regions not only significantly influence climate change but also are highly sensitive to meteorological and climatic conditions (Kammen and

33 Sunter, 2016). Among various meteorological parameters, wind speed exerts great impacts on both environmental and
34 human systems. One prominent example is that wind speed is a crucial consideration for assessing the atmospheric pollutant
35 dispersion capability (Manju et al., 2002; Han et al., 2017). Specifically, mean flows and atmospheric turbulence are two key
36 factors for pollutant removal from urban areas (Wong and Liu, 2013; Di Nicola et al., 2022). Also, wind speed regulates
37 pollen dispersion and distribution that are associated with public health (Roy et al., 2023). The utilization of wind energy in
38 built-up areas also depends on wind speed distribution (Ishugah et al., 2014; Stathopoulos et al., 2018; Tasneem et al., 2020).
39 Proper utilization, through measures such as suburban wind farms or building-integrated turbines, can minimize the need for
40 transmission infrastructure. Beyond energy considerations, wind speed characteristics play a critical role in urban design and
41 planning, influencing both contemporary building practices (Hadavi and Pasdarshahri, 2020) and the preservation of
42 historical-cultural heritage (Li, Y. et al., 2023). Therefore, accurately characterizing wind speed is essential for guiding
43 systematic regulation and promoting sustainable development in built-up areas.

44 Aerodynamic roughness length (z_0) is a crucial parameter that determines near-surface wind speed profiles (Stull, 1988). As
45 a key input for atmospheric models, z_0 significantly influences wind speed-related applications, however, its representation
46 in existing numerical models often oversimplifies real-world conditions. Specifically, most of models, such as the widely
47 used ECMWF Reanalysis v5 (ERA5), determine z_0 with fixed values based on vegetation cover types. Such treatment fails
48 to reflect the impact of various surfaces, especially complex urban structures, posing significant challenges for accurate wind
49 speed simulation and prediction over built-up areas (Wang et al., 2024). Numerous studies have demonstrated that the
50 changes of z_0 , caused by land use changes, particularly urbanization and industrialization, significantly impacted wind speed.
51 For instance, the increase in z_0 has explained 70% of the wind speed reduction in Europe (Wever, 2012) and caused a 1.1
52 m/s decrease in eastern China (Wu et al., 2018). Furthermore, Zhang et al. (2019) identified z_0 changes as a primary driver
53 of long-term wind speed trends in China, Europe, and North America. In line with these findings, Luu et al. (2023) showed
54 that the rise in z_0 , caused by shifts from short vegetation to high vegetation and urbanization, partly contributes to the decline
55 in mean and maximum surface wind speed over Western Europe. These findings highlight the need to refine z_0 in models by
56 incorporating the effects of built-up areas. In addition to wind speed, z_0 also plays a significant role in urban environmental
57 processes. The difference in z_0 between urban and suburban areas is one of drivers causing larger intensity of daytime urban
58 heat islands in humid regions (Zhao et al., 2014; Li et al., 2019). Therefore, accurate z_0 data in built-up areas can not only
59 enhance the performance of atmospheric numerical models, but also provide scientific support for formulating sustainable
60 urban environmental management strategies.

61 The estimation of z_0 in built-up areas traditionally relies on three primary approaches: the micrometeorological method, the
62 morphometric method, and a combination of these two methods. The micrometeorological method, based on the Monin-
63 Obukhov similarity theory (Monin and Obukhov, 1954), typically calculates z_0 using observations from flux or anemometer
64 towers (Grimmond et al., 1998; Liu et al., 2018). Although theoretically robust, this method is limited by high costs of
65 instruments and infrastructure (Grimmond and Oke, 1999), as well as the need for homogeneous surface conditions
66 (Wieringa, 1993; Bottema and Mestayer, 1998). The morphometric method usually formulates mathematical models based

on geometric characteristics and distribution density of built-up areas (Raupach, 1992 and 1994; Bottema and Mestayer, 1998; Macdonald et al., 1998; Kanda et al., 2013; Shen et al., 2022; Shen et al., 2024). However, these models often suffer from simplified assumptions and require high-resolution surface feature data, which are costly to acquire (Grimmond and Oke, 1999; Zhang et al., 2017). The combination method, which establishes a relationship between the z_0 ground truth obtained from micrometeorological method and high-resolution surface feature data for regional-scale applications, has shown promise in specific regions, such as Tokyo and Nagoya (Kanda et al., 2013), Beijing (Zhang et al., 2017), and Osaka subregions (Duan and Takemi, 2021). Nevertheless, the limitations of the former two methods hinder its broader applications. Therefore, there is a considerable lack of reliable z_0 data in built-up regions.

To address the aforementioned challenges, this study proposed a low-cost method for estimating z_0 by integrating 10-m wind speed at China Meteorological Administration (CMA) stations with 10-m wind speed and z_0 from ERA5 reanalysis data. This approach takes advantage of the synergy between CMA's high-density station distribution and ERA5 reanalysis' temporal continuity to substantially enhance the sample size of z_0 estimates. Based on these estimates, we have developed a high-resolution monthly z_0 dataset for built-up areas in China using Random Forest Regression (RFR) algorithm. The applicability of the new z_0 dataset have been assessed through its implementation in the Weather Research and Forecasting (WRF) model for wind speed simulation. This study contributes to the advancement of mesoscale wind speed simulation over built-up environments, which can promote wind field-dependent studies, such as urban planning, wind energy utilization, and air quality management.

2 Data and Method

2.1 Data

In this study, we mainly utilized monthly gridded z_0 dataset from ERA5 (Hersbach et al., 2020 and 2023a), referred to as z_{0_ERA5} , along with hourly 10-m wind speed data from both ERA5 (Hersbach et al., 2023b) and surface weather station observations provided by the China Meteorological Administration (CMA) during 2015-2019, to derive z_0 estimates at each CMA station.

To extend the site-scale z_0 estimates into a gridded dataset at the regional scale, we applied the RFR algorithm, incorporating six key features: variance of the slope ($\overline{\theta^2}$), terrain standard deviation within 0.01° window (TSD), percent tree cover (PTC), leaf area index (LAI), normalized difference vegetation index ($NDVI$), and urban-rural classification (URC). $\overline{\theta^2}$ was derived as an integral over orographic spectrum, capturing multi-scale orographic complexity with wave length from meter to 10 km (Beljaars et al., 2004). TSD was calculated using elevation data from Shuttle Radar Topography Mission with a spatial resolution of 3 arcseconds (Jarvis et al., 2018). The PTC data were obtained from the MOD44B Version 6.1 Vegetation Continuous Fields product (DiMiceli et al., 2022), which provides yearly data at a 250-meter pixel resolution. The monthly 1-km $NDVI$ data were acquired from MOD13A3 product (Didan, 2021). The LAI data with an 8-day temporal interval and

500-meter spatial resolution were sourced from Yuan et al. (2011) and Lin et al. (2023). *URC* data were extracted from a 1-km global human settlements map, which categorizes the rural-urban continuum into 19 distinct types (Li, X. et al., 2022 and 2023). To generate a monthly z_0 dataset at a spatial resolution of $0.01^\circ \times 0.01^\circ$, all input datasets were linearly interpolated or resampled to the target resolution. *LAI* data were averaged monthly by assigning each 8-day interval to the closest month. Additionally, to compare with the existed z_0 datasets, a latest z_0 dataset developed by Peng et al. (2022) (denoted as z_{0_peng}) was used by integrating it into the WRF model for wind speed simulation. This dataset was generated by applying machine learning techniques to integrate FLUXNET ground-based observations and MODIS remote sensing data. Moreover, 100-m wind speed data from 589 anemometer towers in China were utilized for two critical purposes. First, the comparison between tower observations and ERA5 100-m wind speed data (Hersbach et al., 2023b) was used to validate the feasibility of the assumption in the z_0 estimation method. Second, tower data were used as independent validations to evaluate the impact of refined z_0 on wind speed simulations. These anemometer towers cover varying periods between 2004 and 2022 with a temporal resolution of 10 min.

2.2 Method for deriving z_0 at CMA stations

First, the theoretical basis for deriving z_0 at CMA stations is presented. In the framework of Monin-Obukhov similarity theory (Monin and Obukhov, 1954), the neutral logarithmic wind profile can be expressed with Equation (1).

$$u_z = \frac{u_*}{k} \ln \left(\frac{z - d}{z_0} \right) \quad (1)$$

where u_z is the wind speed (m/s) at height z , the measuring height above ground (m); u_* is the friction velocity (m/s); k is the von Karman constant and equals to 0.4, and d is the zero-plane displacement height (m), calculated as $d = 20/3 z_0$ using a widely accepted empirical formula (Watts et al., 2000).

Based on Equation (1), the 100-m neutral wind speed for ERA5 and CMA stations can be expressed in Equations (2) and (3), respectively.

$$u_{100_ERA5} = u_{10_ERA5} \frac{\ln \left(\frac{100 - d_{ERA5}}{z_{0_ERA5}} \right)}{\ln \left(\frac{10 - d_{ERA5}}{z_{0_ERA5}} \right)} \quad (2)$$

$$u_{100_CMA} = u_{10_CMA} \frac{\ln \left(\frac{100 - d_{CMA}}{z_{0_CMA}} \right)}{\ln \left(\frac{10 - d_{CMA}}{z_{0_CMA}} \right)} \quad (3)$$

And then z_0 values at CMA stations can be estimated by the following three steps:

First, we assumed: (1) the near-surface wind speed difference between ERA5 and CMA is primarily attributed to z_0 , and the influence of z_0 diminishes with height. Consequently, the 100-m wind speed from ERA5 reanalysis is considered comparable to that from observations; (2) the impact of atmospheric stability on wind speed is identical for both ERA5 and

125 CMA stations, allowing us to neglect stability correction terms under non-neutral conditions when deriving z_0 for each
126 hourly interval. The validity of these assumptions will be supported by the subsequent validation of wind speed simulations
127 based on the derived z_0 values (Section 3.3).

128 Second, we calculated the hourly z_{0_CMA} values based on Equations (2) and (3). Given that u_{10_ERA5} , u_{10_CMA} , and z_{0_ERA5}
129 values are known, an optimal z_{0_CMA} value at each hour was derived through minimizing the difference between u_{100_ERA5}
130 and u_{100_CMA} calculated using Equations (2) and (3). To align with Assumption (1), we only retained z_{0_CMA} values
131 corresponding to times when the percentage difference between the calculated u_{100_ERA5} and u_{100_CMA} was less than 10%.

132 Third, these retained z_{0_CMA} values were grouped by months, and the monthly median values were selected as the final
133 roughness length ($z_{0_optimal}$). To avoid unreasonable estimates, the values of $z_{0_optimal}$ satisfying the condition that the
134 absolute difference between $\ln z_{0_optimal}$ and the corresponding $\ln z_{0_ERA5}$ does not exceed 2 were considered valid.

135 Finally, we obtained monthly z_0 estimates at 1,805 stations out of the 2,162 CMA stations.

136 2.3 Method for estimating gridded z_0 at regional scale

137 Machine learning serves as an effective tool for extending the $z_{0_optimal}$ estimates at CMA stations to the regional scale. In
138 this study, we employed the RFR algorithm (Equation (4)) (Breiman, 2001), a widely used method for similar applications
139 (Duan and Takemi, 2021; Hu et al., 2022; Peng et al., 2022 and 2023). All samples were divided into training and test subsets
140 at a ratio of 8:2 for each bin of $\ln z_{0_optimal}$, with the bins defined at intervals of 0.2. Sensitivity tests were conducted to
141 determine the optimal number of decision trees in the RFR algorithm (Fig. 3b), resulting in the selection of 300 trees. The
142 maximum depth of the trees was set to 18, and the minimum sample split was set to 5. Five-fold cross-validation shows the
143 stable performance (Fig. 3d). Furthermore, the training and test results exhibit minimal sensitivity to the randomization seed
144 used for dataset splitting (Fig. 3a). The resulting gridded aerodynamic roughness length data are referred to as z_{0_RFR} .

$$145 \quad \ln z_0 = f(\overline{\theta^2}, TSD, PTC, LAI, NDVI, URC, month) \quad (4)$$

146 2.4 Model configuration

147 To demonstrate the applicability of gridded z_{0_RFR} data, the WRF (Version 4.0) Model (Skamarock et al., 2019) was used in
148 this study to simulate wind speed with z_{0_RFR} . For comparison, two additional simulations were performed: one utilized the
149 WRF model's default roughness length ($z_{0_Default}$) based on land cover types, and the other used z_{0_Peng} .

150 First, we set z_{0_RFR} and z_{0_Peng} in WRF model, respectively. Given that z_{0_RFR} is concentrated in built-up areas, the missing
151 values over other regions are filled with $z_{0_Default}$. Notably, the setting of z_{0_Peng} in WRF is different from that of z_{0_RFR} . In
152 the WRF model, z_0 values over bare fraction and vegetated fraction are determined separately. Specifically, in the Noah-MP
153 land surface model, z_0 is set to a constant over bare areas, while it is assigned by a look-up table according to vegetation type

over vegetated areas. Peng et al. (2022) only provided the z_0 over vegetation areas, which is the gridded mean effective roughness length including vegetated fraction and bare fraction. Thus, before conducting the simulation of wind speed in the WRF model with the gridded z_{0_Peng} , we adjusted the roughness length over vegetated fraction in each grid from z_{0_Peng} . The specific adjustment of z_{0_Peng} in the WRF model is comprehensively described in the supplementary material Section 1. Apart from the difference in the sources of z_0 , other model configurations for z_{0_RFR} , $z_{0_Default}$, and z_{0_Peng} are identical. The specific model configurations are as follows.

The simulation domains were configured with a “lat-lon” map projection, centered at coordinates 31.5°N, 109.0°E. As illustrated in Fig. 4b, nested domains were employed, with horizontal resolutions of 0.09° for Domain 1 (d01) and 0.03° for Domain 2 (d02). Specifically, d01 consisted of 225 grid points in the west-east direction and 191 in the south-north direction, while d02 consisted of 469 grid points in the west-east direction and 367 in the south-north direction. The vertical level had 70 layers and was stretched with $dzstretch_s = 1.1$ and $dzstretch_u = 1.04$. The model top was set to 50 hPa. The simulation periods spanned from March 31st to April 30th in 2019. The integral time interval was set to 30 seconds. The re-initialization simulation was performed. Specifically, each simulation started at 12:00 local time (LT, LT=UTC+8) and ran for 36 hours until 24:00 LT the next day. The first 12 hours were considered the spin-up time and the remaining hours were used for analysis. Additionally, the initial and boundary conditions in the simulations were taken from hourly ERA5 reanalysis data, which provide pressure-level variables (geopotential height, air temperature, air humidity, and wind field) (Hersbach et al., 2023c) and surface variables (surface air temperature, humidity, pressure, 10 m wind field, sea level pressure, land surface temperature, soil temperature, and soil water content) (Hersbach et al., 2023b).

For physical parameterization schemes, the modified Thompson microphysics scheme (Thompson et al., 2008), Dudhia scheme for shortwave radiation (Dudhia, 1989), Rapid Radiative Transfer Model (RRTM) scheme for longwave radiation (Mlawer et al., 1997), Noah-MP land surface model (Niu et al., 2011), Yonsei University scheme for planetary boundary layer (Hong et al., 2006), and Grell-Freitas for cumulus parameterization (Grell and Freitas, 2013) were adopted. The cumulus parameterization scheme was exclusively activated in the d02 domain. A turbulent orographic form drag scheme with description of the dynamic drag caused by sub-grid orography was also applied (Beljaars et al., 2004; Zhou et al., 2018).

2.5 Calculation of statistical metrics

To evaluate the performance of the simulated wind speed with z_{0_RFR} , $z_{0_Default}$, and z_{0_Peng} , three statistical metrics, including correlation coefficient (R), mean absolute bias (MAB), and root mean square error ($RMSE$), were used in temporal and spatial aspects. For the spatial performance assessment, the average 10-m wind speed simulation during April 1st to 30th in 2019 at each station was used to calculate R , MAB , and $RMSE$ with the CMA observations.

Regarding the temporal evaluation, the *index* (representing R , MAB , and $RMSE$) was calculated as the mean of the corresponding metric for hourly 10-m wind speed during April 1st to 30th in 2019 across all CMA stations (Equation (5)).

185

$$index = \frac{\sum_{i=1}^M index_i}{M} \quad (5)$$

186 where $index_i$ denotes the respective metric value at the i -th station, and M represents the total number of stations.

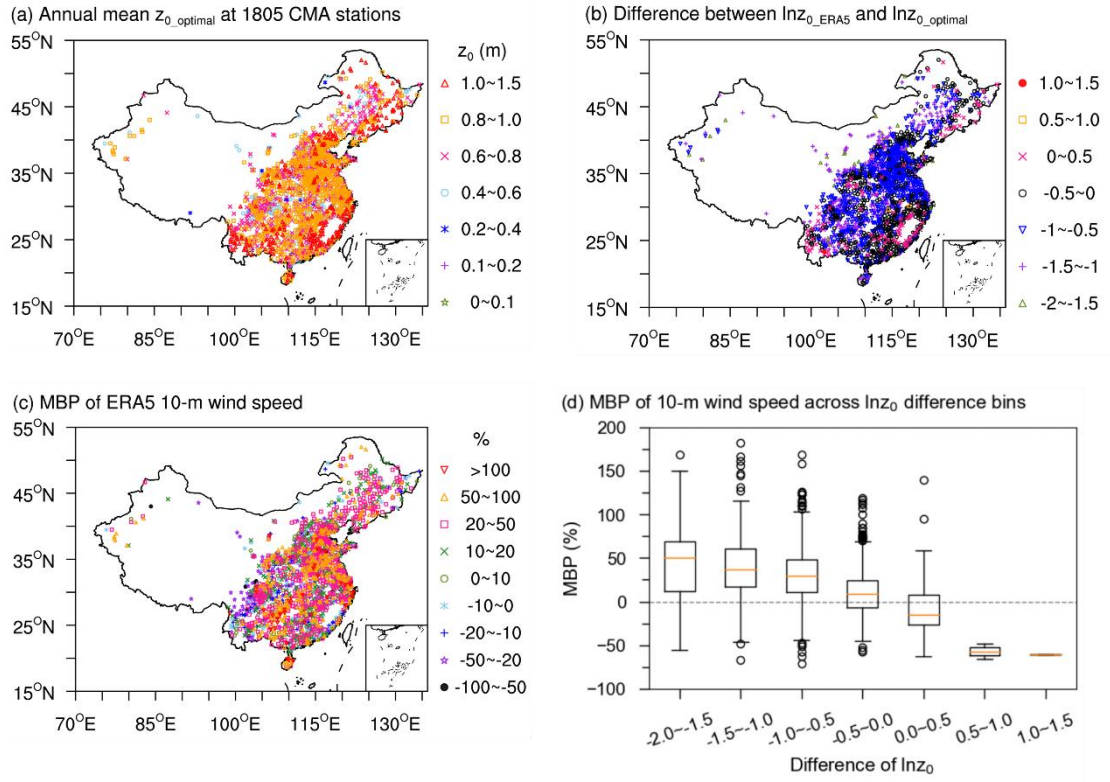
187 3 Results

188 3.1 The distribution characteristics of the z_0 estimates at CMA stations

189 Figure 1a presents the spatial distribution of annual mean $z_{0_optimal}$ values derived from 1,805 CMA stations, representing a
 190 subset of all accessible 2,162 stations (Figure S1). These 1,805 stations are primarily located in the eastern, southern, and
 191 central regions of China, with most stations having z_0 values ranging between 0.6 and 1.5 m. In contrast, the excluded 357
 192 stations are mostly distributed in the western regions of China. The exclusions of these stations can be attributed to the poor
 193 performance of ERA5 100-m wind speed data, which may result from altitude differences between the observation sites and
 194 the model terrain, thereby rendering our initial assumption, i.e. ERA5 100-m wind speed data are reliable for z_0 estimation,
 195 invalid in these areas. To test this, we evaluated the performance of ERA5 100-m wind speed by comparing it with 589
 196 anemometer tower data, since CMA stations only provide 10-m wind speed observations. Overall, ERA5 shows a smaller
 197 mean bias percentage (*MBP*) in the eastern regions compared to the western regions (Fig. 2a). Therefore, the spatial
 198 distribution of the 1,805 stations with valid z_0 values is reasonable.

199 To demonstrate the validity of the estimated z_0 , we analyzed the relationship between z_0 estimates and wind speeds.
 200 Compared to the annual mean $\ln z_{0_optimal}$ derived from 1,805 stations, the $\ln z_{0_ERA5}$ values are systematically lower at most
 201 locations, resulting in positive *MBP* values of 10-m wind speed between ERA5 reanalysis data and station observations (Figs.
 202 1b and 1c). The discrepancies between $\ln z_{0_ERA5}$ and $\ln z_{0_optimal}$ are likely due to rapid urbanization around the majority of
 203 CMA stations, characterized by extensive construction of buildings, which enhances surface roughness and consequently
 204 reduces near-surface wind speeds (Li et al., 2018; Zhang and Wang, 2021). However, the impact of urbanization is likely not
 205 considered in the ERA5 reanalysis. Figures 2b and 2c depict the distribution of CMA stations classified by urban-rural
 206 categories. All stations are situated in built-up areas, with the majority located in urban and town regions, highlighting the
 207 need to incorporate urbanization effects into wind speed simulations to improve model accuracy. In contrast, at a few
 208 locations, where the $\ln z_{0_ERA5}$ values are higher, the corresponding *MBP* values of 10-m wind speed are negative (Figs. 1b
 209 and 1c). The influence of $\ln z_0$ difference on wind speed bias becomes more pronounced as the magnitude of $\ln z_0$ deviation
 210 increases (Fig. 1d). The robust consistency in the relationship between z_0 and wind speed confirms the reasonableness of the
 211 $z_{0_optimal}$, and suggests that improving z_0 values over built-up areas in numerical models could significantly enhance wind
 212 speed simulation accuracy.

213



214

215 **Figure 1.** (a) Spatial distribution of annual mean $z_{0_optimal}$ across 1,805 CMA stations. (b) Difference between annual mean $\ln z_{0_ERA5}$
 216 and $\ln z_{0_optimal}$ (i.e., $\ln z_{0_ERA5}$ minus $\ln z_{0_optimal}$). (c) Mean bias percentage (MBP) of 10-m wind speed between ERA5 and CMA
 217 stations, calculated as $[u_{ERA5} - u_{CMA}]/u_{CMA} \times 100\%$. (d) Boxplots illustrating the statistical distribution of the MBP for 10-m wind
 218 speed shown in (c) across different intervals of $\ln z_0$ difference shown in (b).

219

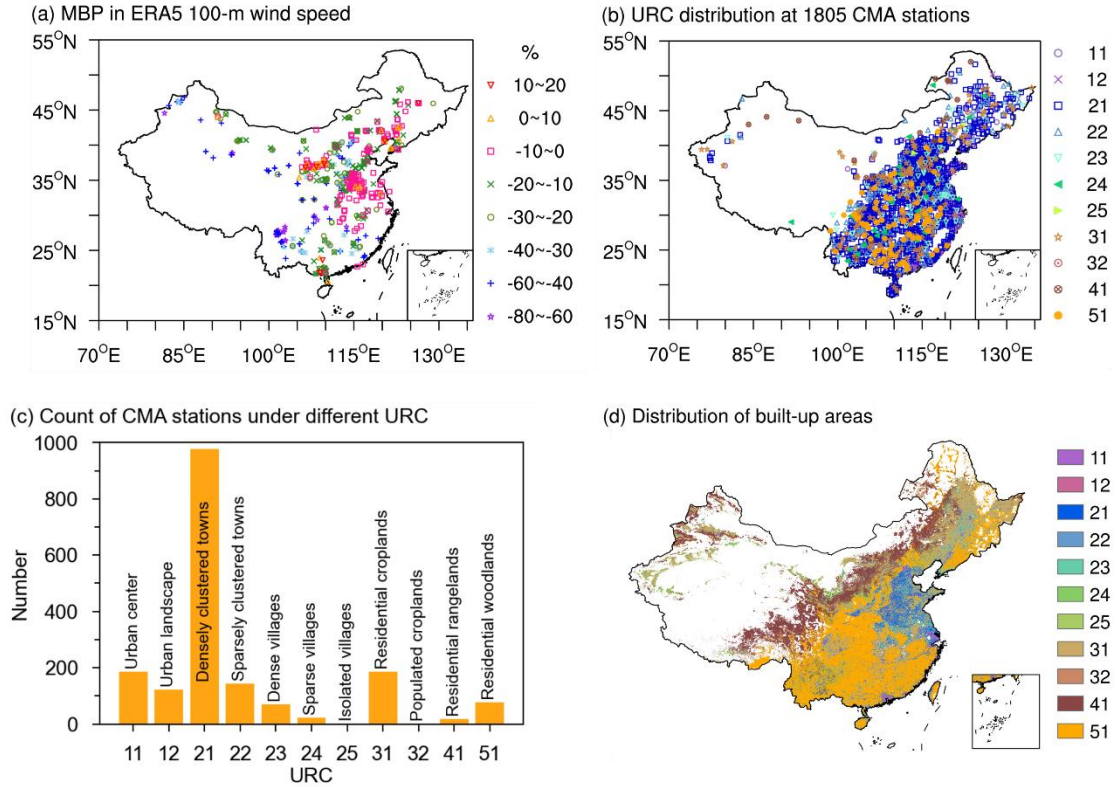
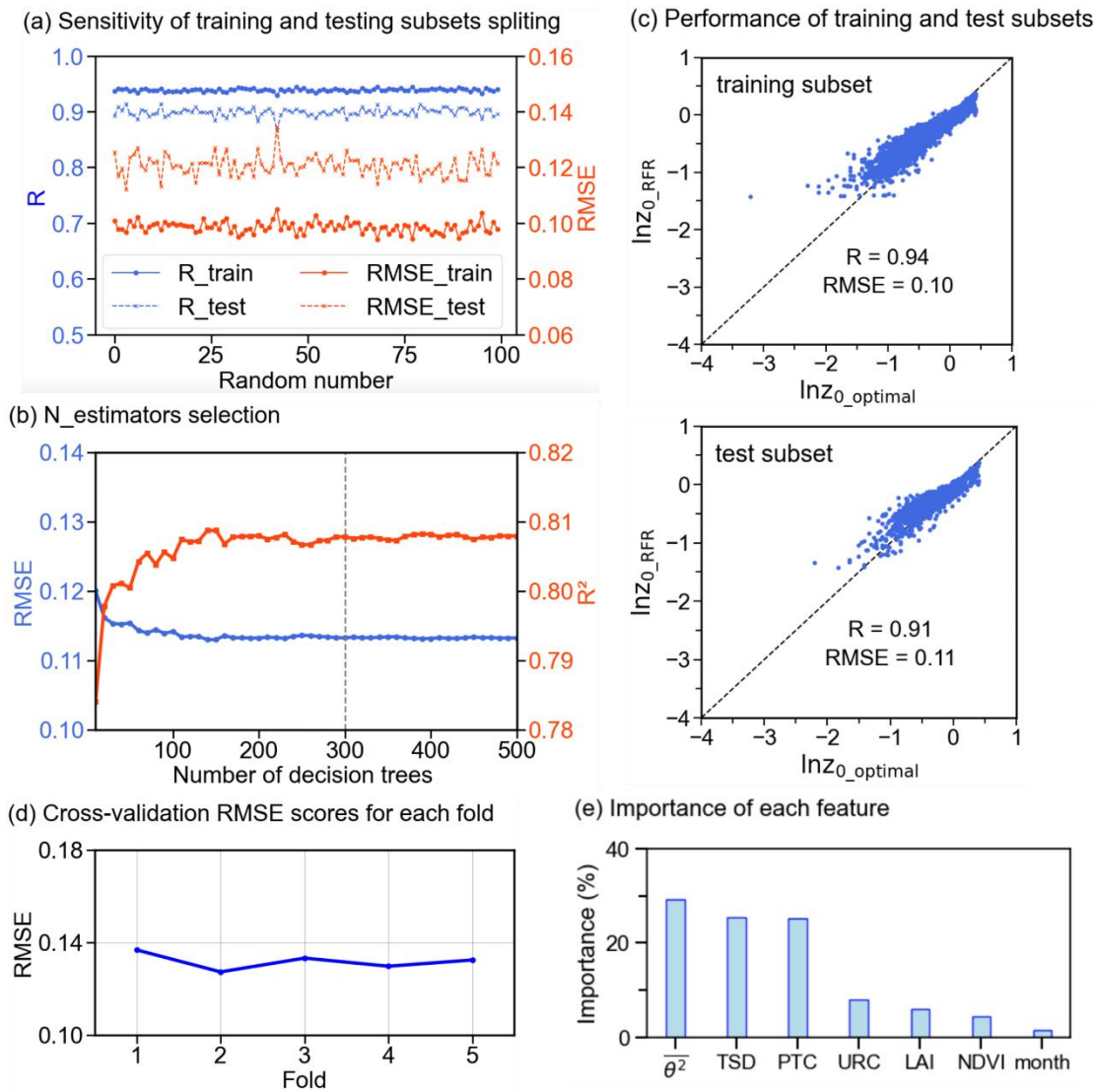


Figure 2. (a) MBP of 100-m wind speed between ERA5 and 589 anemometer towers, calculated as $[u_{ERA5} - u_{tower}]/u_{tower} \times 100\%$. (b) Spatial distribution of urban-rural classification (URC) at 1,805 CMA stations. The legend on the right indicates the URC codes, with the corresponding URC types labeled in panel (c). (c) Number of CMA stations for each URC. The numerical labels on the x-axis represent the URC codes, with the specific URC types annotated on the bars. (d) Spatial distribution of built-up areas across China, and the built-up areas are composed of the 11 types covered by CMA stations in panel (b).

3.2 Development of a gridded z_0 dataset in built-up areas across China

To demonstrate the reliability and practicality of the estimated $z_{0_optimal}$, we constructed a gridded z_0 dataset based on these estimations in order to apply it in numerical simulations. Given that the estimated z_0 values from 1,805 stations are located within built-up areas consisting of 11 distinct types (Figs. 2b and 2c), this study developed a monthly gridded z_0 dataset specifically for these categories of areas with a spatial resolution of $0.01^\circ \times 0.01^\circ$ using the RFR algorithm, referred to as z_{0_RFR} . As a representative example, the z_{0_RFR} dataset was generated for the year 2019, and its spatial coverage is shown in Fig. 2d. Six feature variables closely related to z_0 were used as inputs, encompassing topographic characteristics ($\bar{\theta}^2$ and TSD), vegetation conditions (PTC , LAI , and $NDVI$), and urban-rural distribution (URC). Figure 3c shows that the RFR algorithm exhibits satisfactory performance on both training and test subsets. Feature importance analysis reveals that topographic features and PTC exert the most significant influence on $\ln z_{0_RFR}$ (Fig. 3e). Although 2019 was chosen for

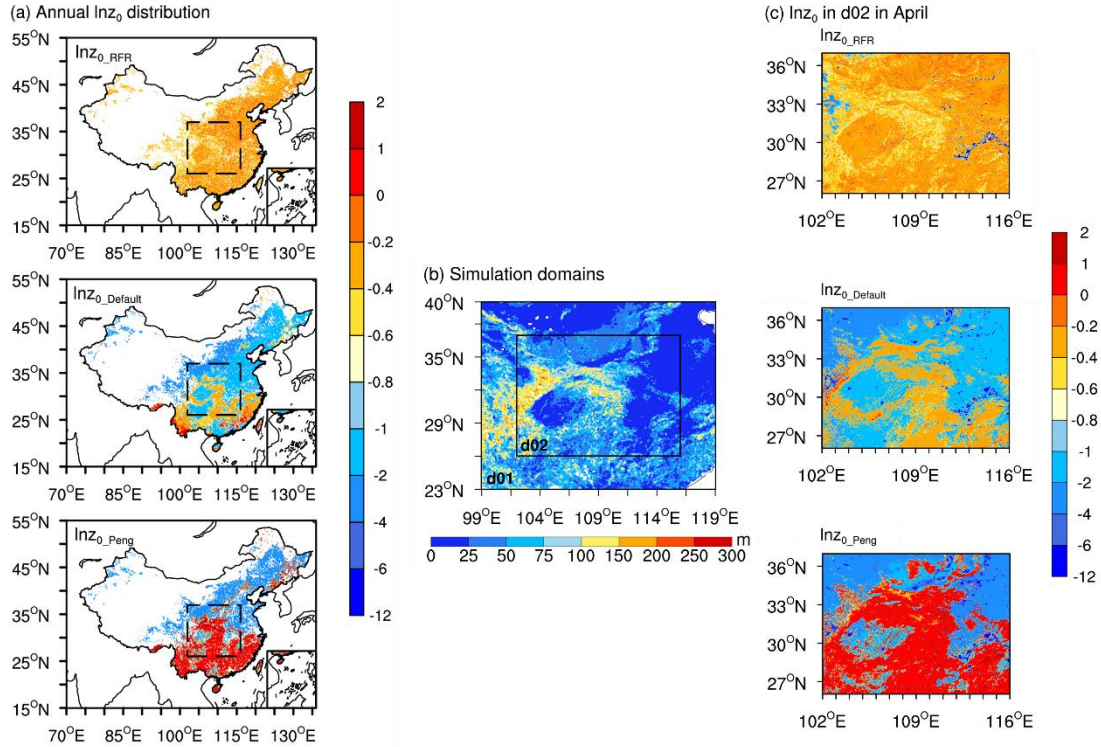
236 demonstration, the RFR model itself is year-independent and can be applied to other years, provided that the required input
 237 features are available.



238
 239 **Figure 3.** Sensitivity analysis and performance evaluation of the Random Forest Regression (RFR) algorithm. (a) Sensitivity of RFR
 240 results to the randomization seed for training and test subsets splitting. R and $RMSE$ represent correlation coefficient and root mean square
 241 error, respectively. (b) Determination of the optimal number of decision trees. R^2 represents determination coefficient. (c) Performance of
 242 the RFR algorithm on the training and test subsets. The R and $RMSE$ values are displayed. (d) Performance evaluation using five-fold
 243 cross-validation. (e) Importance scores of different feature variables.

244 The spatial distribution of $\ln Z_{0_RFR}$ shows limited monthly variability (Fig. S2). The most pronounced monthly variations
 245 occur predominantly in the surrounding areas of the Sichuan Basin, likely due to the prevalence of residential woodlands in
 246 these regions that have seasonal variations in vegetation structure and biomass. The annual mean spatial distribution of

247 $\ln z_{0_RFR}$, with values in built-up areas generally falling within the range of -1 to 0, exhibits distinct patterns compared to
 248 $\ln z_{0_Default}$ and $\ln z_{0_Peng}$ (Fig. 4a). In comparison with $\ln z_{0_Default}$ and $\ln z_{0_Peng}$, $\ln z_{0_RFR}$ shows a more homogeneous
 249 spatial distribution pattern across China. Specifically, in northern China, $\ln z_{0_RFR}$ values are consistently higher than those of
 250 both $\ln z_{0_Default}$ and $\ln z_{0_Peng}$, with $\ln z_{0_Default}$ generally higher than $\ln z_{0_Peng}$. Conversely, in southern China, $\ln z_{0_Peng}$
 251 values are significantly higher than both $\ln z_{0_Default}$ and $\ln z_{0_RFR}$. However, in southeastern and southwestern China,
 252 $\ln z_{0_Default}$ values exceed those of $\ln z_{0_RFR}$, while in the remaining southern areas, $\ln z_{0_RFR}$ maintains higher values
 253 compared to $\ln z_{0_Default}$.



254
 255 **Figure 4.** (a) Spatial distributions of annual mean $\ln z_{0_RFR}$, $\ln z_{0_Default}$, and $\ln z_{0_Peng}$. The dashed rectangular box indicates the
 256 simulation domain (d02) in panel (b). (b) Nested simulation domains (d01: outer domain; d02: inner domain) with terrain standard
 257 deviation within 0.01° window (TSD) represented by color shading. (c) Spatial distributions of $\ln z_0$ used in simulations over d02 in April.

258 3.3 Application of the produced z_0 datasets in wind speed simulation

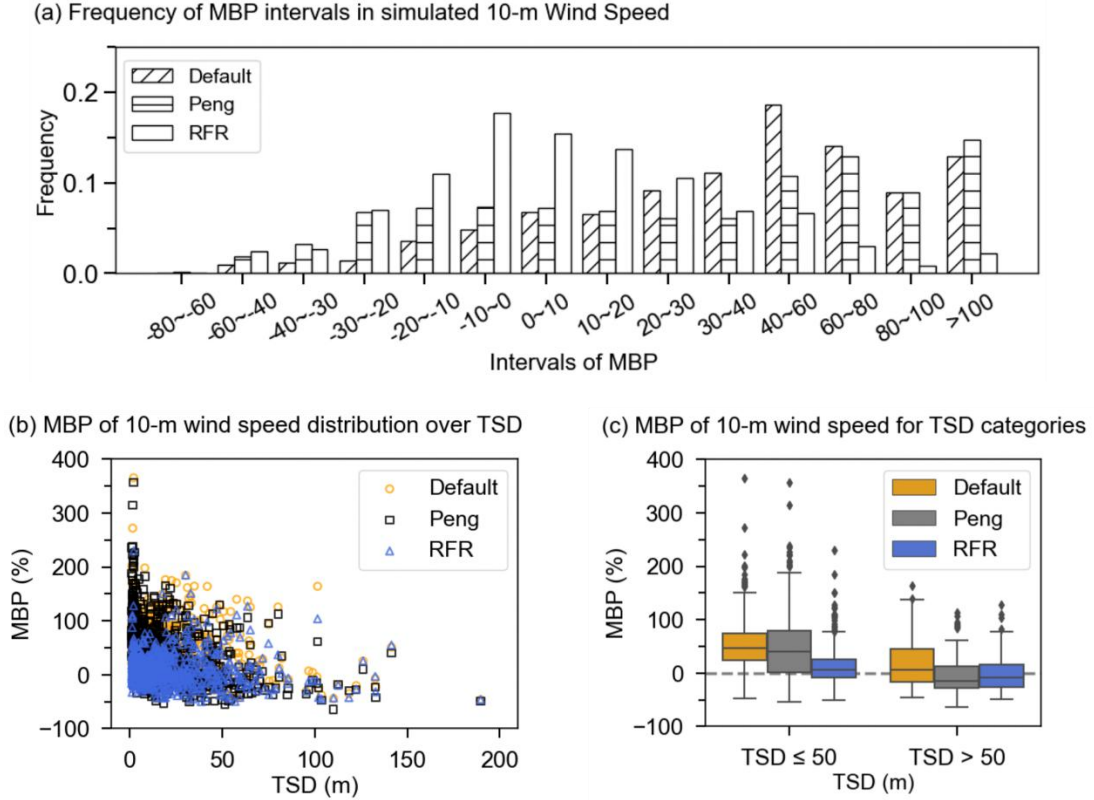
259 To evaluate the performance of $\ln z_{0_RFR}$, we implemented it in the WRF model for wind speed simulations, as z_0 directly
 260 affects near-surface wind speed. A 3-km simulation for April 2019 was conducted using the WRF model with z_{0_RFR} over
 261 the regions outlined in Fig. 4a, which correspond to the d02 domain in Fig. 4b and represent the primary areas of z_{0_RFR}
 262 concentration. April was selected because it is the month with the highest average wind speed in the target domain (Fig. S3),

thus better reflecting the impact of z_0 on wind speed. For comparison, two additional simulations were performed: one utilizing the WRF model's default roughness length ($z_{0_Default}$) based on land cover types, and the other employing a recent z_0 dataset (z_{0_Peng}). In the northeastern, northern, and western regions of the d02 domain, both $\ln z_{0_Default}$ and $\ln z_{0_Peng}$ are generally lower than $\ln z_{0_RFR}$ estimates, with $\ln z_{0_Peng}$ having even lower values than $\ln z_{0_Default}$ (Fig. 4c). However, this pattern reverses in the southeastern areas and along the surrounding area of the Sichuan Basin, where both $\ln z_{0_Default}$ and $\ln z_{0_Peng}$ surpass $\ln z_{0_RFR}$ estimates, and notably, with $\ln z_{0_Peng}$ having significantly higher values than $\ln z_{0_Default}$ in these regions. These discrepancies in z_0 would inevitably directly affect the accuracy of wind speed simulation. To evaluate the influence, we conducted a comprehensive assessment on both 10-m and 100-m wind speed simulations, which represent typical heights for meteorological observations and wind energy applications, respectively.

3.3.1 Evaluation of the simulated 10-m wind speed

We first compared the simulated 10-m wind speed with observations from 753 CMA stations in study areas (d02 domain), showing that z_{0_RFR} significantly enhances the accuracy of simulations. The improvement due to z_{0_RFR} is evident in the smaller *MBP* values of the simulated wind speed (Figures 5a and S4) and the closer alignment of average wind speed with observational data (Fig. 6a). Specifically, the frequency histogram of *MBP* values reveals that the simulation results using z_{0_RFR} mostly fall within an absolute *MBP* range of less than 30%, with a substantial proportion concentrated below 10%. In contrast, simulations employing $z_{0_Default}$ display a majority of *MBP* values exceeding 30%, while simulations using z_{0_Peng} are even poorer, with a larger number of stations falling within higher *MBP* ranges (Fig. 5a). The improvement in 10-m wind speed induced by z_{0_RFR} is primarily evident in relatively flat regions. As *TSD* increases, the improvement gradually diminishes (Fig. 5b). z_{0_RFR} outperforms both $z_{0_Default}$ and z_{0_Peng} when *TSD* does not exceed 50 m, while it shows superior performance to $z_{0_Default}$ and comparable results to z_{0_Peng} when *TSD* > 50 m (Fig. 5c). Spatially, significant improvements are observed in the relatively flat eastern and northern study areas, whereas limited enhancements are found in regions with higher *TSD* surrounding the Sichuan Basin (Fig. S4). The limited improvement in relatively complex terrain arises because, in addition to z_0 , wind speed over these regions is influenced by multi-scale factors, including microscale terrain features (Ge et al., 2025), turbulent orographic form drags (Beljaars et al., 2004; Jiménez and Dudhia, 2011; Zhou et al., 2018), surface heating-induced mountain-valley circulations (Kim et al., 2021), mountain waves (Draxl, et al., 2021) and other processes. Inaccurate parameterizations of these factors in numerical models can all lead to errors in wind speed simulations. For the mean 10-m wind speed, simulations using z_{0_RFR} (2.17 m/s) show better agreement with the CMA observations (2.08 m/s), whereas simulations with $z_{0_Default}$ and z_{0_Peng} show greater overestimations, producing mean wind speeds of 2.97 m/s and 2.89 m/s, respectively (Fig. 6a and Table 1). In other words, z_{0_RFR} decreases mean bias of 10-m wind speed by 89.9% and 88.9% compared to $z_{0_Default}$ and z_{0_Peng} , respectively. Independent validations across 155 stations (Fig. 6b), from the

294 test subset in the generation of z_{0_RFR} , further confirm the superiority of z_{0_RFR} (Fig. 6a). In addition, the improvements in
 295 10-m wind speed were observed throughout the entire simulation period (Fig. 6c). Note that our experimental design,
 296 employing a re-initialization strategy, means that 30 independent simulation experiments were conducted in April. Thus,
 297 although the simulations were only conducted for a month, the consistent improvement across all days shows that the
 298 enhancement achieved by z_{0_RFR} is robust. Moreover, the statistical metrics also show that the simulated 10-m wind speed
 299 using z_{0_RFR} outperforms those using $z_{0_Default}$ and z_{0_Peng} in temporal and spatial *MAB* and *RMSE* (Fig. 6d).



300
 301 **Figure 5.** (a) Frequency distribution of *MBP* in simulated 10-m wind speed in April using $z_{0_Default}$, z_{0_Peng} , and z_{0_RFR} against
 302 observations from CMA stations. *MBP* was calculated as $[u_{simulations} - u_{CMA}]/u_{CMA} \times 100\%$. (b) Distribution of *MBP* in 10-m wind
 303 speed as a function of *TSD*. (c) Box plot of *MBP* in 10-m wind speed across different *TSD* bins.

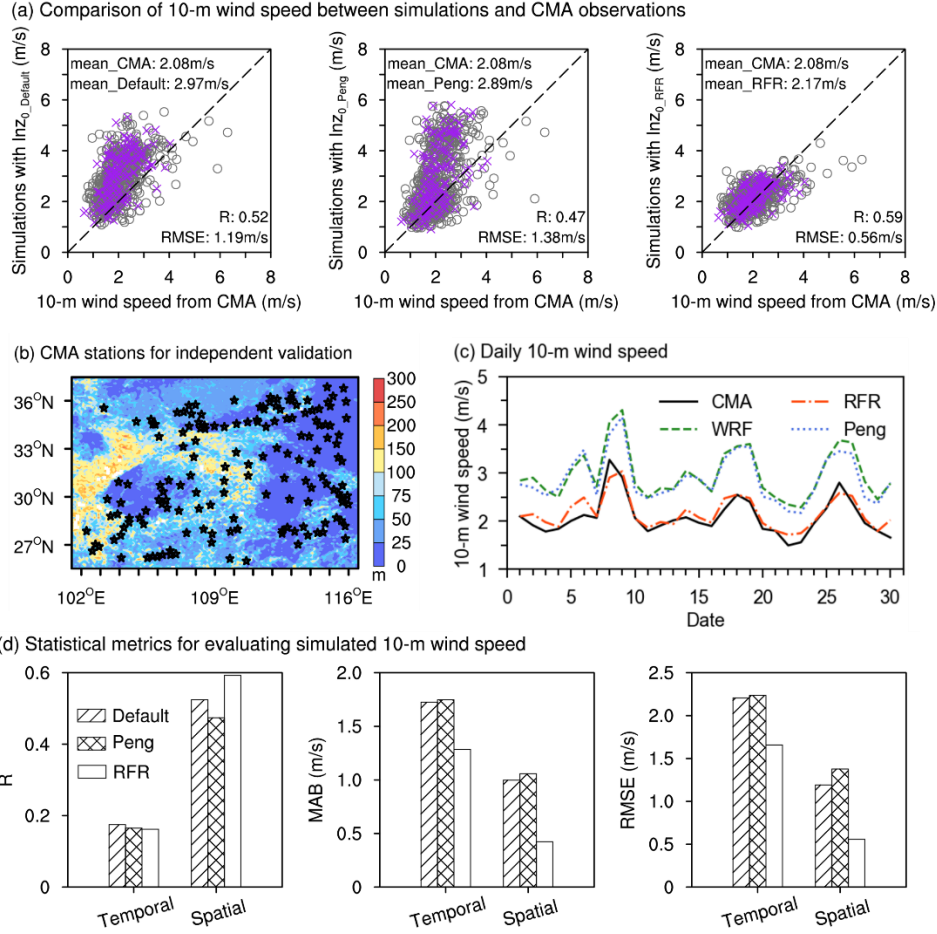


Figure 6. (a) Comparisons of mean 10-m wind speed in April between the simulations using $z_{0_Default}$, z_{0_Peng} , and z_{0_RFR} versus observations from CMA stations. All points (grey circles and purple crosses) represent the 753 CMA stations within the d02 domain available for comparison, while the purple crosses represent the 155 stations utilized for independent validation, which were not used in training the z_{0_RFR} model. The corresponding wind speed means, correlation coefficients (R), and root mean square errors ($RMSE$) of all stations are also indicated. (b) Distribution of the 155 independent CMA stations (black stars). Colored shaded areas represent TSD . (c) Comparison of daily mean 10-m wind speed between simulations and observations from 753 CMA stations. (d) Statistical metrics comparing simulated and observed 10-m wind speeds, including temporal and spatial R , mean absolute bias (MAB , $\frac{1}{N} \sum_{i=1}^N |u_i^{simulation} - u_i^{observation}|$), where N represents the number of hours for temporal MAB , and the number of stations for spatial MAB) and $RMSE$.

Table 1. The mean 10-m wind speed from simulations and observations at 753 CMA stations, and the mean 100-m wind speed from simulations and observations at 50 anemometer towers. The simulations were conducted using $z_{0_Default}$, z_{0_Peng} , and z_{0_RFR} , respectively. The percentage reduction in wind speed error is caused by z_{0_RFR} , compared to $z_{0_Default}$ and z_{0_Peng} , which is calculated as $[\frac{|\bar{u}_{z_{0_Default}} - \bar{u}_{observation}| - |\bar{u}_{z_{0_RFR}} - \bar{u}_{observation}|}{|\bar{u}_{z_{0_Default}} - \bar{u}_{observation}|} \times 100\%$, where $\bar{u}_{z_{0_*}}$ represents $\bar{u}_{z_{0_Default}}$ or $\bar{u}_{z_{0_Peng}}$, and \bar{u}

denotes the mean 10-m or 100-m wind speed from simulations based on $z_{0_Default}$, z_{0_Peng} , and z_{0_RFR} , as well as from observations (CMA stations or anemometer towers).

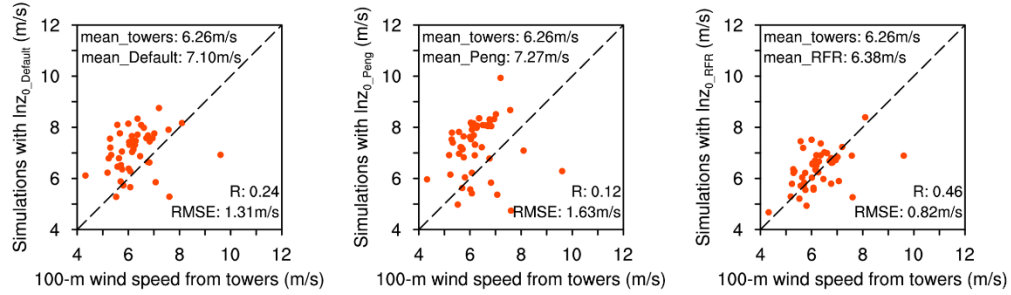
	$z_{0_Default}$	z_{0_Peng}	z_{0_RFR}	Observations
Mean 10-m wind speed (m/s)	2.97	2.89	2.17	2.08
Percentage reduction in 10-m wind speed error caused by z_{0_RFR} (%)	89.9%	88.9%	-	-
Mean 100-m wind speed (m/s)	7.10	7.27	6.38	6.26
Percentage reduction in 100-m wind speed error caused by z_{0_RFR} (%)	85.7%	88.1%	-	-

3.3.2 Evaluation of the simulated 100-m wind speeds

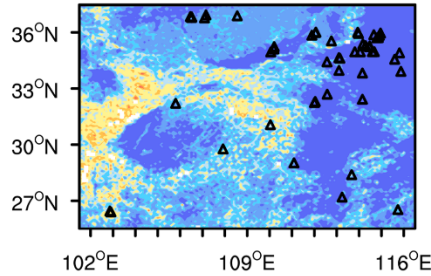
In addition to 10-m wind speed, the simulated 100-m wind speed was also improved through the use of z_{0_RFR} (Fig. 7a and Table 1). Compared to observations from 50 anemometer towers (Fig. 7b), with an average 100-m wind speed of 6.26 m/s, simulations based on $z_{0_Default}$ and z_{0_Peng} overestimate the wind speed, with averages of 7.10 m/s and 7.27 m/s, respectively. However, the mean 100-m wind speed simulated using z_{0_RFR} is 6.38 m/s, closer to the observations (Table 1). This improvement using z_{0_RFR} reduces wind speed mean bias by 85.7% and 88.1% compared to $z_{0_Default}$ and z_{0_Peng} , respectively. Consistent with the performance of z_{0_RFR} at 10-m wind speed, the improvement in 100-m wind speed is more pronounced in relatively flat regions (Fig. 7c). The outliers in Fig. 7a, where wind speed biases remain significant despite using z_{0_RFR} , are located in areas with higher TSD . Furthermore, similar to its performance at 10-m height, z_{0_RFR} demonstrates superior performance in simulated 100-m wind speed across both temporal and spatial metrics, with the exception of the temporal correlation coefficient (Fig. 7d). The relatively lower temporal R is reasonable, as the improvement in wind speed induced by z_0 primarily stems from enhancements in the vertical profile.

In summary, the 30 independent simulation cases conducted for April demonstrate that the z_0 values derived from the combination of CMA observations and ERA5 data are highly reliable. The resulting gridded z_0 dataset significantly reduces uncertainties in mesoscale near-surface wind speed simulations, particularly over relatively flat built-up areas. To further validate the robustness of the z_0 estimation method and the resulting dataset, we conducted additional simulations for October 2019, a month characterized by generally weaker wind conditions (Fig. S3), using the same model configuration as in April. The results (Figs. S5-S7) also show consistent improvements when using z_{0_RFR} , further reinforcing the reliability and applicability of the proposed z_0 estimation approach under varying meteorological conditions.

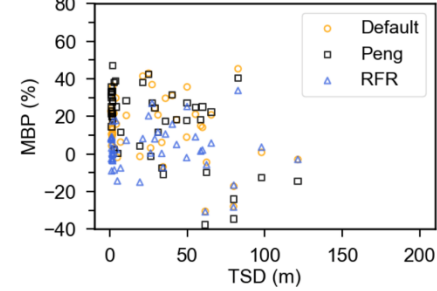
(a) Comparison of 100-m wind speed between simulations and anemometer towers



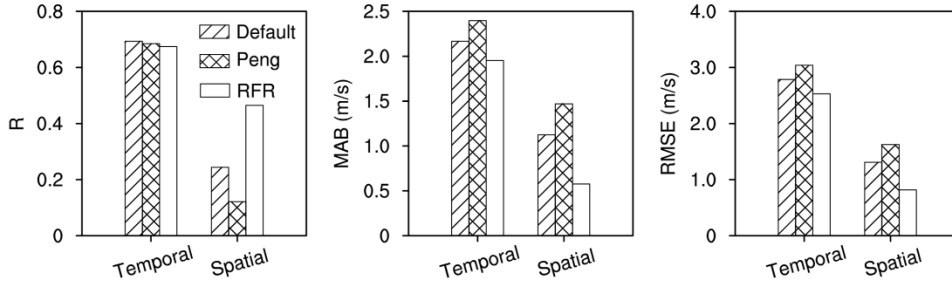
(b) Distribution of anemometer towers



(c) MBP of 100-m wind speed distribution over TSD



(d) Statistical metrics for evaluating simulated 100-m wind speed



339

340 **Figure 7.** (a) Comparisons of mean 100-m wind speed in April between the simulations using $z_{0_Default}$, z_{0_Peng} , and z_{0_RFR} versus
341 observations from anemometer towers. The corresponding wind speed means, R , and $RMSE$ of all towers are also indicated. (b) The
342 locations of 50 anemometer towers (black triangles) utilized for 100-m wind speed evaluation. Colored shaded areas represent TSD . (c)
343 Distribution of MBP in 100-m wind speed as a function of TSD . MBP was calculated as $[u_{simulations} - u_{towers}]/u_{towers} \times 100\%$. (d)
344 Statistical metrics comparing simulated and observed 100-m wind speeds, including temporal and spatial R , MAB , and $RMSE$.

345 4. Discussion

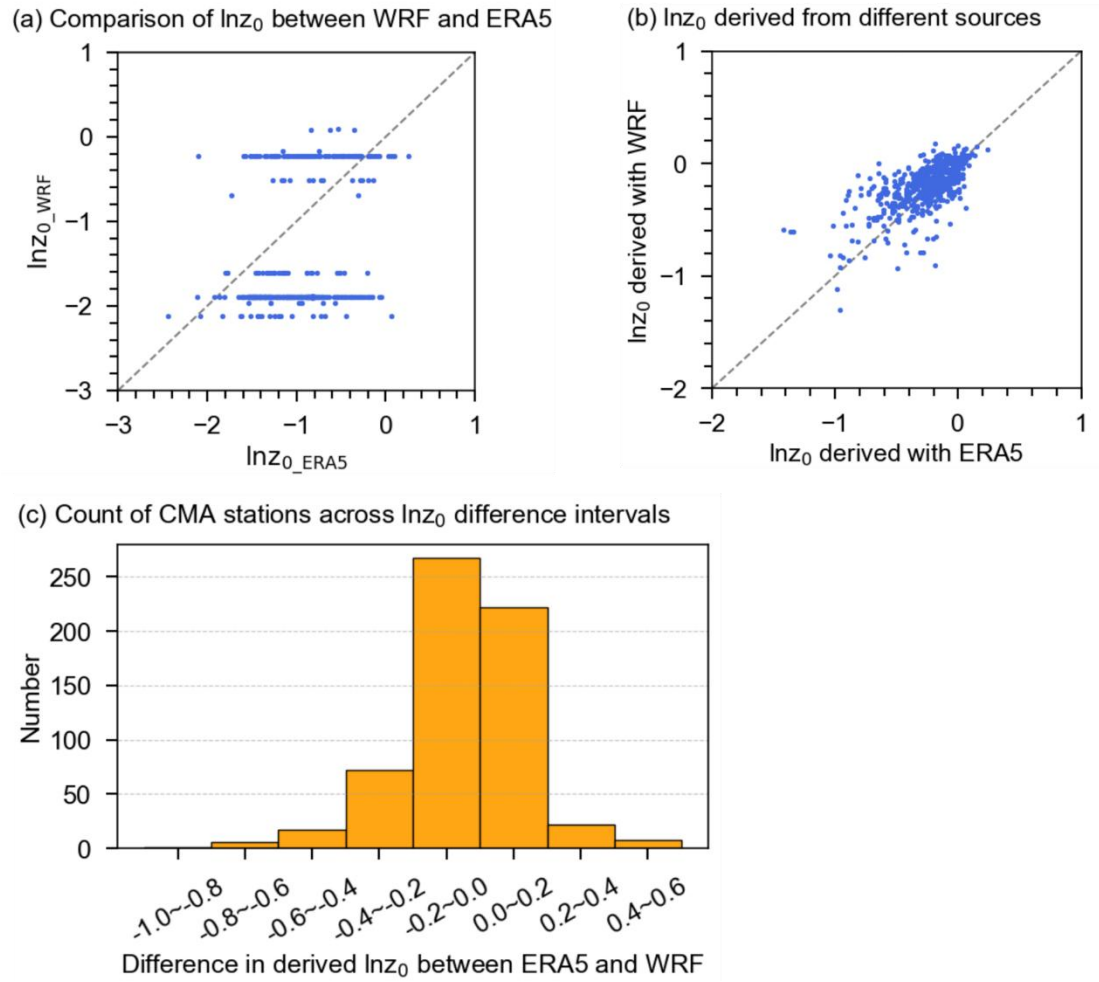
346 Here we discuss the sensitivity and generality of the site z_0 estimation approach with respect to the input simulation or
347 reanalysis data, addressing concerns about potential methodological dependence on ERA5. Our study utilized ERA5
348 reanalysis data and CMA observations for initial z_0 estimation. Compared to traditional meteorological or morphological
349 methods, our approach can provide z_0 values at large spatial coverage and low cost, and these values lead to clear

improvements in WRF-simulated wind speeds at both 10 m and 100 m above ground level. To assess whether the performance gain stems from improved z_0 representation rather than from alignment with ERA5 reanalysis data, we carried out two additional sets of evaluations.

First, we applied the same approach to estimate z_0 from WRF-simulated 10-m wind speed and the model's default z_0 values ($0.03^\circ \times 0.03^\circ$), instead of ERA5. The z_0 values estimated using this alternative dataset were found to be highly similar to those derived from ERA5 (Fig. 8), indicating that the method is not inherently reliant on ERA5 as a data source. The primary advantage of using ERA5 lies in its extensive spatiotemporal coverage, which offers greater convenience and consistency with observational data; however, the methodology itself is general and transferable to other datasets. Moreover, the agreement between ERA5- and WRF-derived z_0 values suggests that the spatial representativeness of the estimated site-level z_0 values is not determined by the resolution of the reanalysis or simulation dataset used, but rather by the measurement height of wind observations at the stations. In this study, 10-m wind speeds from CMA stations were used. As a rule of thumb, the horizontal representativeness of wind measurements is approximately 100 times the measurement height. Therefore, z_0 values estimated from 10-m wind observations are reasonably representative at ~ 1 km scales, making the generation of 0.01° gridded z_0 datasets for use in mesoscale simulations both appropriate and justified.

Second, we further validated the robustness of the refined z_0 dataset (z_{0_RFR}) by conducting additional WRF simulations driven by the reanalysis from National Centers for Environmental Prediction (NCEP) instead of ERA5. These results (Fig. S8 and Table S1) still showed significant improvement in wind speed simulation performance when using z_{0_RFR} , consistent with those driven by ERA5. This cross-reanalysis consistency demonstrates that the benefits are attributable to the improved surface representation through z_{0_RFR} refinement, not simply tuning to match ERA5-driven wind fields.

Taken together, these findings confirm that the z_0 estimation method proposed in this study is robust, flexible, and not dependent on alignment with a specific reanalysis dataset. It provides a practical framework for z_0 estimation that can be widely applied across different reanalysis/simulation datasets and observational data with consistent benefits. However, this method is limited in regions with sparse or no surface weather stations. Notably, these regions, such as western and northern China, are rich in wind resources and are key targets for wind energy development. Therefore, producing high-quality gridded z_0 datasets in these regions warrants further study by exploring alternative data sources, such as anemometer tower wind profiles, to supplement z_0 truth values (Wang et al., 2024).



376

377 **Figure 8.** (a) Comparison of $\ln z_0$ values from default WRF model ($\ln z_{0_WRF}$) and ERA5 ($\ln z_{0_ERA5}$). (b) Comparison of $\ln z_0$ estimates
 378 using different datasets. $\ln z_0$ derived from WRF represents the estimated values based on WRF simulations (10-m wind speed and default
 379 z_0) and CMA station observations (10-m wind speed) during April 2019, while $\ln z_0$ derived from ERA5 denotes the estimates obtained in
 380 this study using ERA5 reanalysis data in April. (c) Distribution of station counts across intervals of the difference in derived $\ln z_0$ ($\ln z_0$
 381 derived from ERA5 minus $\ln z_0$ derived from WRF).

382 5. Conclusion

383 The representation of z_0 in numerical models, typically determined by vegetation types, may lead to significant uncertainties
 384 in wind speed simulations and predictions. Traditional methods for obtaining z_0 ground truth are mainly constrained by high
 385 costs. In this study, we proposed a low-cost z_0 estimation method, allowing the acquisition of z_0 values at routine weather
 386 stations.

Specifically, this approach leverages 10-m wind speed and z_0 values from ERA5 reanalysis data, along with observed 10-m wind speeds at CMA stations, to derive optimal z_0 at stations by minimizing the difference in 100-m wind speeds between reanalysis and observations. Here, the 100-m wind speed is expressed with 10-m wind speed and z_0 using similarity theory. Based on this approach, we derived z_0 values at 1,805 CMA stations out of a total of 2,162 stations. These stations are located in built-up regions, indicating the estimated z_0 values inherently include the effects of urbanization and industrialization.

To validate the reliability and practicality of the estimation method, we utilized a Random Forest Regression algorithm, incorporating feature variables closely related to z_0 , to develop a monthly gridded z_0 dataset for built-up areas in China with a spatial resolution of $0.01^\circ \times 0.01^\circ$. The resulting $\ln z_0$ values mainly range from -1 to 0. Simulations with WRF model show that, compared to the default z_0 in WRF and a recent gridded z_0 dataset developed by Peng et al. (2022), the z_0 dataset constructed in this study has significantly improved the accuracy of near-surface wind speed simulations in built-up areas, particularly in relatively flat regions. Evaluations against independent weather station data and anemometer tower data show simulations with the new z_0 dataset mitigates mean bias of 10-m wind speed by 89.9% and 88.9%, and mean bias of 100-m wind speed by 85.7% and 88.1%, respectively, compared to the default z_0 in WRF and the z_0 dataset from Peng et al. (2022). In summary, this study developed a simple yet effective approach for correcting model z_0 , addressing the limitations of relying on empirical values assigned based on vegetation cover types. The method shows particular effectiveness in z_0 correction for built-up areas and offers valuable support for wind field-dependent studies and applications.

Code and data availability.

- Code required to conduct the analyses herein is available at <https://doi.org/10.5281/zenodo.15108200> (Wang, 2025).

The datasets used in this study fall into two categories based on their accessibility:

1. Publicly Available Datasets (accessible via DOI/URL).

- The hourly wind speed data at 10 m and 100 m heights are obtained from the ERA5 reanalysis dataset (Hersbach et al., 2020), accessible at <https://doi.org/10.24381/cds.adbb2d47> (Hersbach et al., 2023b).
- For the gridded datasets of z_0 used in this study, z_{0_ERA5} (Hersbach et al., 2020) is available at <https://doi.org/10.24381/cds.fl7050d7> (Hersbach et al., 2023a), while z_{0_Peng} (Peng et al., 2022) can be acquired by contacting the corresponding authors.
- The initial and boundary conditions for the simulations are from the ERA5 dataset (Hersbach et al., 2020), which can be downloaded from <https://doi.org/10.24381/cds.adbb2d47> (Hersbach et al., 2023b) and <https://doi.org/10.24381/cds.bd0915c6> (Hersbach et al., 2023c).
- The digital elevation data, with a spatial resolution of 3 arc-seconds, are sourced from the Shuttle Radar Topography Mission (SRTM) and can be downloaded from <https://csidotinfo.wordpress.com/data/srtm-90m-digital-elevation-database-v4-1/> (Jarvis et al., 2008).
- The urban-rural classification data (Li, X. et al., 2023) are available at <https://doi.org/10.6084/m9.figshare.21716357.v6> (Li et al., 2022).
- The variance of the slope ($\overline{\theta^2}$) data can be obtained by contacting Zhou et al. (2018).
- The Leaf Area Index (LAI) data (Lin et al., 2023; Yuan et al., 2011) are accessible at <http://globalchange.bnu.edu.cn/research/laiv061> (Beijing Normal University Global Change Data Archive, 2022).
- The percent tree cover data (DiMiceli et al., 2022) can be obtained from <https://doi.org/10.5067/MODIS/MOD44B.061>

and [https://search.earthdata.nasa.gov/search/granules?p=C2565805839-LPCLOUD&pg\[0\]\[v\]=f&pg\[0\]\[gsk\]=-start_date&q=MOD44B&tl=1733462795.688!3!!&lat=-0.140625](https://search.earthdata.nasa.gov/search/granules?p=C2565805839-LPCLOUD&pg[0][v]=f&pg[0][gsk]=-start_date&q=MOD44B&tl=1733462795.688!3!!&lat=-0.140625) (NASA EOSDIS, 2024a).

- The NDVI data (Didan, 2021) are available from <https://doi.org/10.5067/MODIS/MOD13A3.061> and [https://search.earthdata.nasa.gov/search/granules?p=C2327962326-LPCLOUD&pg\[0\]\[v\]=f&pg\[0\]\[gsk\]=-start_date&q=MOD13A3&tl=1732851935.718!3!!&lat=-0.140625](https://search.earthdata.nasa.gov/search/granules?p=C2327962326-LPCLOUD&pg[0][v]=f&pg[0][gsk]=-start_date&q=MOD13A3&tl=1732851935.718!3!!&lat=-0.140625) (NASA EOSDIS, 2024b).
- The NCEP forcing data (National Centers for Environmental Prediction/National Weather Service/NOAA/U.S. Department of Commerce, 2025) are available from <https://rda.ucar.edu/datasets/d083002/dataaccess/>.

2. Restricted Datasets. We would like to clarify that the meteorological station data from the China Meteorological Administration (CMA) and the anemometer tower data used in this study are not publicly accessible but can be accessed through the following way. Specifically:

- The data from anemometer towers are provided by China State Shipbuilding Corporation Haizhuang Windpower Co., Ltd., however, they are not accessible publicly because of their commercial interests. These data can be obtained by cooperation with the company.
- The hourly 10-m wind speed data at meteorological stations are from the China Meteorological Administration (CMA). In accordance with the data policy of China, these data record are not directly accessible for public download via a website. Nevertheless, individuals interested in obtaining detailed information about data acquisition can reach out to the China Meteorological Data Service Center at their official website (<http://data.cma.cn/en/?r=data/detail&dataCode=A.0012.0001>, China meteorological data service centre, 2023).

Author contributions. All authors contributed to the study. JW and KY conceived the study and conducted the design; JW, KY, and JL carried out data analyses; JW, XZ and XM performed the configuration of WRF model; WT processed data from CMA stations; LY provided the data from anemometer towers; ZR conducted data collection and cleaning of anemometer towers; JW and KY wrote the manuscript; all authors discussed, reviewed and edited the manuscript.

Competing interests. The contact author has declared that none of the authors has any competing interests.

Disclaimer. Publisher's note: Copernicus Publications remains neutral with regard to jurisdictional claims in published maps and institutional affiliations.

Financial support. This work was supported by the National Natural Science Foundation of China (Grant Nos. 42475138 and 42361144875).

References

- Beljaars, A., Brown, A. R. and Wood, N: A new parametrization of turbulent orographic form drag, Q. J. R. Meteorol. Soc., 130, 1327-1347, doi:10.1256/qj.03.73, 2010.
- Beijing Normal University Global Change Data Archive: Leaf Area Index (LAI) Dataset [data set], <http://globalchange.bnu.edu.cn/research/laiv061>, last access: 24 March 2022.
- Breiman, L.: Random forests, Mach. Learn., 45, 5-32, doi:10.1023/A:1010933404324, 2001.
- Bottema, M. and Mestayer, P. G.: Urban roughness mapping - Validation techniques and some first results, J. Wind Eng. Ind. Aerodyn., 74-76, 163-173, doi:10.1016/S0167-6105(98)00014-2, 1998.

China meteorological data service centre: Daily Timed Data from automated weather stations in China [data set],
<http://data.cma.cn/en/?r=data/detail&dataCode=A.0012.0001>, last access: 6 May 2023.

Di Nicola, F., Brattich, E. and Di Sabatino, S.: A new approach for roughness representation within urban dispersion models, *Atmos. Environ.*, 283, 119181, doi:10.1016/j.atmosenv.2022.119181, 2022.

Didan, K.: MODIS/Terra Vegetation Indices Monthly L3 Global 1km SIN Grid V061, NASA EOSDIS Land Processes Distributed Active Archive Center [data set], doi:10.5067/MODIS/MOD13A3.061.

DiMiceli, C., Sohlberg, R. and Townshend, J.: MODIS/Terra Vegetation Continuous Fields Yearly L3 Global 250m SIN Grid V061, NASA EOSDIS Land Processes Distributed Active Archive Center [data set], doi:10.5067/MODIS/MOD44B.061, 2022.

Draxl, C., Worsnop, R. P., Xia, G., Pichugina, Y., Chand, D., Lundquist, J. K., Sharp, J., Wedam, G., Wilczak, J. M., and Berg, L. K.: Mountain waves can impact wind power generation, *Wind Energ. Sci.*, 6, 45-60, doi:10.5194/wes-6-45-2021, 2021.

Duan, G. and Takemi, T.: Predicting urban surface roughness aerodynamic parameters using random forest, *J. Appl. Meteorol. Climatol.*, 60, 999-1018, doi:10.1175/JAMC-D-20-0266.1, 2021.

Dudhia, J.: Numerical study of convection observed during the winter monsoon experiment using a mesoscale two-dimensional model, *J. Atmos. Sci.*, 46, 3077-3107, doi:10.1175/1520-0469(1989)046<3077:NSOCOD>2.0.CO;2, 1989.

Ge, C., Yan, J., Song, W., Zhang, H., Wang, H., Li, Y. and Liu, Y.: Middle-term wind power forecasting method based on long-span NWP and microscale terrain fusion correction, *Renew. Energy*, 240, 122123, doi:10.1016/j.renene.2024.122123, 2025.

Grell, G. A. and Freitas, S. R.: A scale and aerosol aware stochastic convective parameterization for weather and air quality modeling, *Atmos. Chem. Phys.*, 14, 5233-5250, doi:10.5194/acpd-13-23845-2013, 2014.

Grimmond, C. S. B., King, T. S., Roth, M. and Oke, T. R.: Aerodynamic roughness of urban areas derived from wind observations, *Bound.-Layer Meteorol.*, 89, 1-24, doi:10.1023/A:1001525622213, 1998.

Grimmond, C. S. B. and Oke, T. R.: Aerodynamic properties of urban areas derived from analysis of surface form, *J. Appl. Meteorol. Climatol.*, 38, 1262-1292, doi:10.1175/1520-0450(1999)038<1262:APOUAD>2.0.CO;2, 1999.

Hadavi, M. and Pasharshahi, H.: Quantifying impacts of wind speed and urban neighborhood layout on the infiltration rate of residential buildings, *Sustain. Cities Soc.*, 53, 101887, doi:10.1016/j.scs.2019.101887, 2020.

Han, Z., Zhou, B., Xu, Y., Wu, J. and Shi, Y.: Projected changes in haze pollution potential in China: an ensemble of regional climate model simulations, *Atmos. Chem. Phys.*, 17, 10109-10123, doi:10.5194/acp-17-10109-2017, 2017.

Hersbach, H., Bell, B., Berrisford, P., Biavati, G., Horányi, A., Muñoz Sabater, J., Nicolas, J., Peubey, C., Radu, R., Rozum, I., Schepers, D., Simmons, A., Soci, C., Dee, D. and Thépaut, J.-N.: ERA5 monthly averaged data on single levels from 1940 to present, Copernicus Climate Change Service (C3S) Climate Data Store (CDS) [data set], doi:10.24381/cds.f17050d7, 2023a.

499 Hersbach, H., Bell, B., Berrisford, P., Biavati, G., Horányi, A., Muñoz Sabater, J., Nicolas, J., Peubey, C., Radu, R., Rozum,
 500 I., Schepers, D., Simmons, A., Soci, C., Dee, D. and Thépaut, J.-N.: ERA5 hourly data on single levels from 1940 to present,
 501 Copernicus Climate Change Service (C3S) Climate Data Store (CDS) [data set], doi:10.24381/cds.adbb2d47, 2023b.
 502 Hersbach, H., Bell, B., Berrisford, P., Biavati, G., Horányi, A., Muñoz Sabater, J., et al.: ERA5 hourly data on pressure
 503 levels from 1940 to present, Copernicus Climate Change Service (C3S) Climate Data Store (CDS) [data set],
 504 doi:10.24381/cds.bd0915c6, 2023c.
 505 Hersbach, H., Bell, B., Berrisford, P., Hirahara, S., Horányi, A., Muñoz-Sabater, J., Nicolas, J., Peubey, C., Radu, R.,
 506 Schepers, D., Simmons, A., Soci, C., Abdalla, S., Abellan, X., Balsamo, G., Bechtold, P., Biavati, G., Bidlot, J., Bonavita,
 507 M., De Chiara, G., Dahlgren, P., Dee, D., Diamantakis, M., Dragani, R., Flemming, J., Forbes, R., Fuentes, M., Geer, A.,
 508 Haimberger, L., Healy, S., Hogan, R. J., Hólm, E., Janisková, M., Keeley, S., Laloyaux, P., Lopez, P., Lupu, C., Radnoti, G.,
 509 de Rosnay, P., Rozum, I., Vamborg, F., Villaume, S., and Thépaut, J.-N.: The ERA5 global reanalysis, *Q. J. R. Meteorol.*
 510 *Soc.*, 146, 1999-2049, doi:10.1002/qj.3803, 2020.
 511 Hong, S. Y., Noh, Y. and Dudhia, J.: A new vertical diffusion package with an explicit treatment of entrainment processes,
 512 *Mon. Weather Rev.*, 134, 2318-2341, doi:10.1175/MWR3199.1, 2006.
 513 Hu, X., Shi, L., Lin, L. and Magliulo, V.: Improving surface roughness lengths estimation using machine learning algorithms,
 514 *Agric. For. Meteorol.*, 287, 107956, doi:10.1016/j.agrformet.2020.107956, 2020.
 515 Ishugah, T. F., Li, Y., Wang, R. Z. and Kiplagat, J. K.: Advances in wind energy resource exploitation in urban environment:
 516 A review, *Renew. Sustain. Energy Rev.*, 37, 613-626, doi:10.1016/j.rser.2014.05.053, 2014.
 517 Jarvis, A., Reuter, H. I., Nelson, A. and Guevara, E.: Hole-filled SRTM for the globe Version 4, CGIAR-CSI SRTM 90m
 518 Database [data set], <http://srtm.csi.cgiar.org>, 2008.
 519 Jiménez, P. A. and Dudhia, J.: Improving the representation of resolved and unresolved topographic effects on surface wind
 520 in the WRF model, *J. Appl. Meteorol. Climatol.*, 51, 300-316, doi:10.1175/JAMC-D-11-084.1, 2012.
 521 Kammen, D. M. and Sunter, D. A.: City-integrated renewable energy for urban sustainability, *Science*, 352, 922-928,
 522 doi:10.1126/science.aad9302, 2016.
 523 Kanda, M., Inagaki, A., Miyamoto, T., Gryschka, M. and Raasch, S.: A new aerodynamic parametrization for real urban
 524 surfaces, *Bound.-Layer Meteorol.*, 148, 357-377, doi:10.1007/s10546-013-9818-x, 2013.
 525 Kim, G., Lee, J., Lee, M. I. and Kim, D.: Impacts of urbanization on atmospheric circulation and aerosol transport in a
 526 coastal environment simulated by the WRF-Chem coupled with urban canopy model, *Atmos. Environ.*, 249, 118253,
 527 doi:10.1016/j.atmosenv.2021.118253, 2021.
 528 Li, Z., Song, L., Ma, H., Xiao, J., Wang, K. and Chen, L.: Observed surface wind speed declining induced by urbanization in
 529 East China, *Clim. Dyn.*, 50, 735-749, doi:10.1007/s00382-017-3637-6, 2018.
 530 Li, D., Liao, W., Rigden, A. J., Liu, X., Wang, D., Malyshev, S. and Shevliakova, E.: Urban heat island: Aerodynamics or
 531 imperviousness?, *Sci. Adv.*, 5, eaau4299, doi:10.1126/sciadv.aau4299, 2019.

Li, X., Yu, L. and Chen, X.: New insights into urbanization based on global mapping and analysis of human settlements in the rural-urban continuum, *Land*, 12, 1607, doi:10.3390/land12081607, 2023.

Li, X., Yu, L. and Chen, X.: New insights into urbanization based on global mapping and analysis of human settlements in the rural-urban continuum [data set]. figshare. doi:10.6084/m9.figshare.21716357.v6, 2022.

Li, Y., Sun, P. P., Li, A. and Deng, Y.: Wind effect analysis of a high-rise ancient wooden tower with a particular architectural profile via wind tunnel test, *Int. J. Archit. Herit.*, 17, 518-537, doi:10.1080/15583058.2021.1938748, 2023.

Lin, W., Yuan, H., Dong, W., Zhang, S., Liu, S., Wei, N., Lu, X., Wei, Z., Hu, Y. and Dai, Y.: Reprocessed MODIS version 6.1 leaf area index dataset and its evaluation for land surface and climate modeling, *Remote Sens.*, 15, 1780, doi:10.3390/rs15071780, 2023.

Liu, J., Gao, Z., Wang, L., Li, Y. and Gao, C. Y.: The impact of urbanization on wind speed and surface aerodynamic characteristics in Beijing during 1991-2011, *Meteorol. Atmos. Phys.*, 130, 311-324, doi:10.1007/s00703-017-0519-8, 2018.

Liu, Z., He, C., Zhou, Y. and Wu, J.: How much of the world's land has been urbanized, really? A hierarchical framework for avoiding confusion, *Landsc. Ecol.*, 29, 763-771, doi:10.1007/s10980-014-0034-y, 2014.

Luu, L. N., van Meijgaard, E., Philip, S. Y., Kew, S. F., de Baar, J. H. S. and Stepek, A.: Impact of surface roughness changes on surface wind speed over western Europe: A study with the regional climate model RACMO, *J. Geophys. Res.-Atmos.*, 128, e2022JD038426, doi:10.1029/2022JD038426, 2023.

Macdonald, R. W., Griffiths, R. F. and Hall, D. J.: An improved method for the estimation of surface roughness of obstacle arrays, *Atmos. Environ.*, 32, 1857-1864, doi:10.1016/S1352-2310(97)00403-2, 1998.

Manju, N., Balakrishnan, R. and Mani, N.: Assimilative capacity and pollutant dispersion studies for the industrial zone of Manali, *Atmos. Environ.*, 36, 3461-3471, doi:10.1016/S1352-2310(02)00306-0, 2002.

Mlawer, E. J., Taubman, S. J., Brown, P. D., Iacono, M. J. and Clough, S. A.: Radiative transfer for inhomogeneous atmospheres: RRTM, a validated correlated-k model for the longwave, *J. Geophys. Res.*, 102, 16663-16682, doi:10.1029/97JD00237, 1997.

Monin, A. S. and Obukhov, A. M.: Osnovnye zakonomernosti turbulentnogo peremesivaniya v prizemnon sloe atmosfery (Basic laws of turbulent mixing in the atmosphere near the ground), *Dokl. Akad. Nauk SSSR*, 151, 1963-1987, 1954.

NASA EOSDIS: MODIS/Terra Vegetation Continuous Fields Yearly L3 Global 250m SIN Grid V061 [data set], [https://search.earthdata.nasa.gov/search/granules?p=C2565805839-LPCLOUD&pg\[0\]\[v\]=f&pg\[0\]\[gsk\]=-start_date&q=MOD44B&tl=1733462795.68813!!&lat=-0.140625](https://search.earthdata.nasa.gov/search/granules?p=C2565805839-LPCLOUD&pg[0][v]=f&pg[0][gsk]=-start_date&q=MOD44B&tl=1733462795.68813!!&lat=-0.140625), last access: 3 October 2024a.

NASA EOSDIS: MODIS/Terra Vegetation Indices Monthly L3 Global 1km SIN Grid V061 [data set], [https://search.earthdata.nasa.gov/search/granules?p=C2327962326-LPCLOUD&pg\[0\]\[v\]=f&pg\[0\]\[gsk\]=-start_date&q=MOD13A3&tl=1732851935.71813!!&lat=-0.140625](https://search.earthdata.nasa.gov/search/granules?p=C2327962326-LPCLOUD&pg[0][v]=f&pg[0][gsk]=-start_date&q=MOD13A3&tl=1732851935.71813!!&lat=-0.140625), last access: 22 September 2024b.

National Centers for Environmental Prediction/National Weather Service/NOAA/U.S. Department of Commerce. 2000, updated daily. *NCEP FNL Operational Model Global Tropospheric Analyses, continuing from July 1999* [data set]. Research

565 Data Archive at the National Center for Atmospheric Research, Computational and Information Systems Laboratory.
 566 <https://doi.org/10.5065/D6M043C6>. Accessed 28 May 2025.

567 Niu, G. Y., Yang, Z. L. and Mitchell, K. E.: The community Noah land surface model with multiparameterization options
 568 (Noah-MP): 1. Model description and evaluation with local-scale measurements, *J. Geophys. Res.-Atmos.*, 116, D12109,
 569 doi:10.1029/2010JD015139, 2011.

570 Peng, Z., Tang, R., Jiang, Y., Liu, M. and Li, Z. L.: Global estimates of 500 m daily aerodynamic roughness length from
 571 MODIS data, *ISPRS J. Photogramm. Remote Sens.*, 183, 336-351, doi:10.1016/j.isprsjprs.2021.11.015, 2022.

572 Peng, Z., Tang, R., Liu, M., Jiang, Y. and Li, Z. L.: Coupled estimation of global 500m daily aerodynamic roughness length,
 573 zero-plane displacement height and canopy height, *Agric. For. Meteorol.*, 342, 109754,
 574 doi:10.1016/j.agrformet.2023.109754, 2023.

575 Raupach, M. R.: Drag and drag partition on rough surfaces, *Bound.-Layer Meteorol.*, 60, 375-395, doi:10.1007/BF00155203,
 576 1992.

577 Raupach, M. R.: Simplified expressions for vegetation roughness length and zero-plane displacement as functions of canopy
 578 height and area index, *Bound.-Layer Meteorol.*, 71, 211-216, doi:10.1007/BF00709229, 1994.

579 Roy, P., Chen, L. W. A., Chen, Y. T., Ahmad, S., Khan, E. and Buttner, M.: Pollen dispersion and deposition in real-world
 580 urban settings: A computational fluid dynamic study, *Aerosol Sci. Eng.*, 7, 543-555, doi:10.1007/s41810-023-00198-1, 2023.

581 Shen, C., Shen, A., Cui, Y., Chen, X., Liu, Y., Fan, Q., Chan, P., Tian, C., Wang, C., Lan, J., Gao, M., Li, X. and Wu, J.:
 582 Spatializing the roughness length of heterogeneous urban underlying surfaces to improve the WRF simulation-part 1: A
 583 review of morphological methods and model evaluation, *Atmos. Environ.*, 270, 118874,
 584 doi:10.1016/j.atmosenv.2021.118874, 2022.

585 Shen, G., Zheng, S., Jiang, Y., Zhou, W. and Zhu, D.: An improved method for calculating urban ground roughness
 586 considering the length and angle of upwind sector, *Build. Environ.*, 266, 112144, doi:10.1016/j.buildenv.2024.112144, 2024.

587 Skamarock, W. C., Klemp, J. B., Dudhia, J., Gill, D. O., Liu, Z., Berner, J., Wang, W., Powers, J. G., Duda, M. G., Barker,
 588 D. M. and Huang, X.-Y.: A description of the advanced research WRF model version 4 Rep (Vol. 145). National Center for
 589 Atmos Res National Center for Atmospheric Research. doi:[10.5065/1DFH-6P97](https://doi.org/10.5065/1DFH-6P97), 2019.

590 Stathopoulos, T., Alrawashdeh, H., Al-Quraan, A., Blocken, B., Dilimulati, A., Paraschivoiu, M. and Pilay, P.: Urban wind
 591 energy: Some views on potential and challenges, *J. Wind Eng. Ind. Aerodyn.*, 179, 146-157,
 592 doi:10.1016/j.jweia.2018.05.018, 2018.

593 Stull, R. B.: An introduction to boundary layer meteorology, Springer Science & Business Media, 1988.

594 Tasneem, Z., Noman, A. A., Das, S. K., Saha, D. K., Islam, M. R., Ali, M. F., Badal, M. F. R., Ahamed, M. H., Moyeen, S. I.
 595 and Alam, F.: An analytical review on the evaluation of wind resource and wind turbine for urban application: Prospect and
 596 challenges, *Dev. Built Environ.*, 4, 100033, doi:10.1016/j.dibe.2020.100033, 2020.

597 Thompson, G., Field, P. R., Rasmussen, R. M. and Hall, W. D.: Explicit forecasts of winter precipitation using an improved
 598 bulk microphysics scheme. Part II: implementation of a new snow parameterization, *Mon. Weather Rev.*, 136, 5095-5115,
 599 doi:10.1175/2008MWR2387.1, 2008.

600 Wang, J.: Codes for manuscript “Improvement of near-surface wind speed modeling through refined aerodynamic roughness
 601 length in built-up regions: implementation and validation in the Weather Research and Forecasting (WRF) model version
 602 4.0”, Zenodo [code], doi: 10.5281/zenodo.15108200, 2025.

603 Wang, J., Yang, K., Yuan, L., Liu, J., Peng, Z., Ren, Z. and Zhou, X.: Deducing aerodynamic roughness length from
 604 abundant anemometer tower data to inform wind resource modeling, *Geophys. Res. Lett.*, 51, e2024GL111056,
 605 doi:10.1029/2024GL111056, 2024.

606 Watts, C. J., Chehbouni, A., Rodriguez, J. C., Kerr, Y. H., Hartogensis, O. and de Bruin, H. A. R.: Comparison of sensible
 607 heat flux estimates using AVHRR with scintillometer measurements over semi-arid grassland in northwest Mexico, *Agric.
 608 For. Meteorol.*, 105, 81-89, doi:10.1016/S0168-1923(00)00188-X, 2000.

609 Wever, N.: Quantifying trends in surface roughness and the effect on surface wind speed observations, *J. Geophys. Res.-
 610 Atmos.*, 117, D11101, doi:10.1029/2011JD017118, 2012.

611 Wieringa, J.: Representative roughness parameters for homogeneous terrain, *Bound.-Layer Meteorol.*, 63, 323-363, 1993.

612 Wong, C. C. and Liu, C. H.: Pollutant plume dispersion in the atmospheric boundary layer over idealized urban roughness,
 613 *Bound.-Layer Meteorol.*, 147, 281-300, doi:10.1007/s10546-012-9785-7, 2013.

614 Wu, J., Zha, J., Zhao, D. and Yang, Q.: Effects of surface friction and turbulent mixing on long-term changes in the near-
 615 surface wind speed over the eastern China plain from 1981 to 2010, *Clim. Dynam.*, 51, 1-15, doi:10.1007/s00382-017-4012-
 616 3, 2017.

617 Yuan, H., Dai, Y., Xiao, Z., Ji, D. and Shangguan, W.: Reprocessing the MODIS leaf area index products for land surface
 618 and climate modelling, *Remote Sens. Environ.*, 115, 1171–1187, doi:10.1016/j.rse.2011.01.001, 2011.

619 Zhang, F., Sha, M., Wang, G., Li, Z. and Shao, Y.: Urban aerodynamic roughness length mapping using multitemporal SAR
 620 data, *Adv. Meteorol.*, 2017, 8958926, doi:10.1155/2017/8958926, 2017.

621 Zhang, Z., Wang, K., Chen, D., Li, J. and Robert, D.: Increase in surface friction dominates the observed surface wind speed
 622 decline during 1973–2014 in the northern hemisphere lands, *J. Climate*, 32, 7421-7435, doi:10.1175/JCLI-D-18-0691.1,
 623 2019.

624 Zhang, Z. and Wang, K.: Quantifying and adjusting the impact of urbanization on the observed surface wind speed over
 625 China from 1985 to 2017, *Fundam. Res.*, 1, 785–791, doi:10.1016/j.fmre.2021.09.006, 2021.

626 Zhao, L., Lee, X., Smith, R. B. and Oleson, K.: Strong contributions of local background climate to urban heat islands,
 627 *Nature*, 511, 216–219, doi:10.1038/nature13462, 2014.

628 Zhou, X., Yang, K. and Wang, Y.: Implementation of a turbulent orographic form drag scheme in WRF and its application to
 629 the Tibetan Plateau, *Clim. Dynam.*, 50, 2443-2455, doi:10.1007/s00382-017-3677-y, 2018.